J. Comb. Chem. **2009,** *11,* 829–834

High-Throughput Continuous Hydrothermal Synthesis of an Entire Nanoceramic Phase Diagram

Xiaole Weng,[†,‡] Jeremy K. Cockcroft,[†] Geoffrey Hyett,[†] Martin Vickers,[†]
Paul Boldrin,[†] Chiu C. Tang,[§] Stephen P. Thompson,[§] Julia E. Parker,[§]
Jonathan C. Knowles,[||] Ihtesham Rehman,[‡] Ivan Parkin,[†] Julian R. G. Evans,[†] and
Jawwad A. Darr*[,†]

Christopher Ingold Laboratories, Department of Chemistry, University College London, 20 Gordon Street, London, WC1H 0AJ, United Kingdom, The School of Engineering and Materials Science, Queen Mary University of London, Mile End Road, London, E1 4NS, United Kingdom, Diamond Light Source Ltd., Diamond House, Harwell Science and Innovation Campus, Didcot, Oxfordshire, OX11 0DE, United Kingdom, and Division of Biomaterials and Tissue Engineering, UCL Eastman Dental Institute, 256 Gray's Inn Road, London, WC1X 8LD, United Kingdom

Received March 10, 2009

A novel High-Throughput Continuous Hydrothermal (HiTCH) flow synthesis reactor was used to make directly and rapidly a 66-sample nanoparticle library (entire phase diagram) of nanocrystalline $Ce_xZr_yY_zO_{2-\delta}$ in less than 12 h. High resolution PXRD data were obtained for the entire heat-treated library (at 1000 °C/1 h) in less than a day using the new robotic beamline I11, located at Diamond Light Source (DLS). This allowed Rietveld-quality powder X-ray diffraction (PXRD) data collection of the entire 66-sample library in <1 day. Consequently, the authors rapidly mapped out phase behavior and sintering behaviors for the entire library. Out of the entire 66-sample heat-treated library, the PXRD data suggests that 43 possess the fluorite structure, of which 30 (out of 36) are ternary compositions. The speed, quantity and quality of data obtained by our new approach, offers an exciting new development which will allow structure−property relationships to be accessed for nanoceramics in much shorter time periods.

Introduction

Nanochemistry is concerned with the syntheses of nanoscale (sub-100-nm diameter) particles with different size, shape, composition, surface structure, and functionality.[1] The properties of new functional single-phase nanomaterials[2] aimed at specific applications (e.g., solar cells, gas sensors, fine chemical catalysis, fuel cells, etc.) are very sensitive to levels of dopant cations because of their influence on point defects.[3] Some of these functional materials display the fluorite structure across a wide range of dopant compositions and applications;[4,5] these include electrolytes in intermediate temperature solid oxide fuel cells for stationary power applications,[6] three-way automotive catalyst supports for cleanup of exhaust gases,[7] homogeneous efficient fuel sources in MOX (mixed U/Pu oxide) nuclear reactors,[8] and immobilization phases for radioactive waste elements.[9]

In certain technological applications of nanoceramics,[10] post synthesis heat-treatments or thermal cycling, may lead to deactivation or a change of properties. This can be caused by loss of surface area resulting from sintering, thermal destabilization into less active phases (phase separation), or deactivation of catalytic surface coatings.[11] Consequently, a great deal of effort has gone into evaluating the structure and thermal stabilities of fluorite-based materials in the region of 1000 °C and above.[12,13] It is well-known that homogeneous doping of M^{3+} cations (e.g., Y^{3+}, Pu^{3+}) into a metal-oxide fluorite structure (such as CeO_2 or UO_2) leads to the formation of oxygen vacancies and other lattice defects, which are very important for oxygen anion mobility, electronic properties, and radiological or thermal phase stability. Hence, synthetic methods, which offer homogeneous doping of metal oxides with consequential extension of fluorite phase boundaries (for nanoparticles), are very much of interest. Binary (or higher) nanoceramics can display a wide range of properties across the phase diagram.[6] However, our understanding of how properties vary with structure and composition for nanoparticles is limited. This is for two reasons: (i) the inability of current synthetic methods to make large numbers of homogeneous crystalline nanoceramics rapidly and (ii) the relatively slow speed at which high-quality analytical data can be acquired (and interpreted) for such nanomaterials. Our development of a High-Throughput Continuous Hydrothermal (HiTCH) flow synthesis reactor was driven by the goal to synthesize a large number of unique nanoceramic samples without contamination between consecutive samples (Figure 1a). A novel HiTCH flow synthesis method is described herein that was used to make directly and rapidly compositionally unique,

---

* To whom correspondence should be addressed. E-mail: j.a.darr@ucl.ac.uk.
[†] University College London.
[‡] Queen Mary University of London.
[§] Diamond Light Source Ltd.
[||] UCL Eastman Dental Institute.

10.1021/cc900041a CCC: $40.75

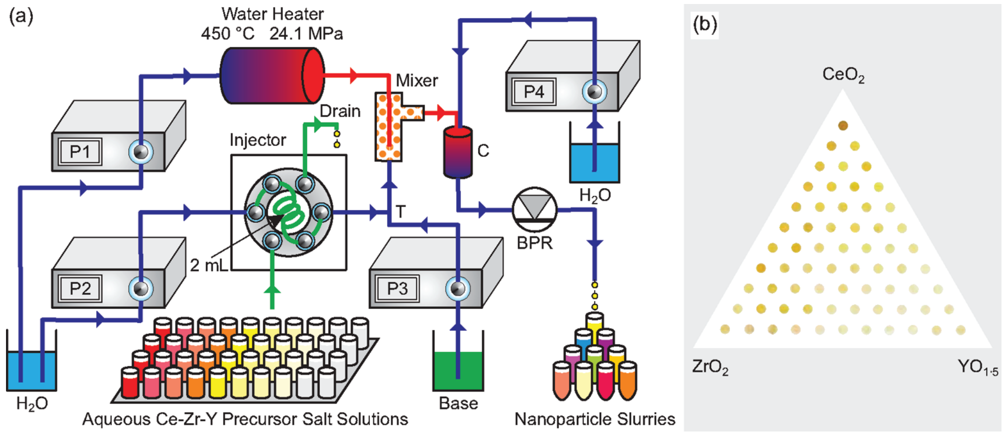

Figure 1. (a) Schematic layout of the high-throughput continuous hydrothermal (HiTCH) flow synthesis system that allows rapid synthesis of compositionally unique crystalline nanoceramic samples at high pressure without contamination between consecutive samples. Each metal salt solution was filled into the loop and upon injection the cold water flow from HPLC pump P2 (5 mL min^{-1}) carried the contents of the loop to a T-piece (T), whereupon it was mixed with a flow of 1 M KOH and 3 vol% H_2O_2 solution that was delivered from pump P3 (5 mL min^{-1}) to give a mixture of pH 14. Thereafter, the mixture was brought to meet a flow of superheated water (via pump P1 at 10 mL min^{-1}) through a heat exchanger to reach 450 °C at the system pressure of 24.1 MPa) at a 1/4" (0.6 cm) counter-current mixer (labeled mixer). The nanoparticle slurries were collected sequentially at the exit of a back-pressure regulator (after cooling). The system was purged with water between concurrent injections and collections. For detailed information on the system and experimental details see Ref S1, Supporting Information. (b) Freeze-dried powders were fired at 1000 °C and filled into a PTFE triangular holder.

high surface-area nanoceramics (Ref S1, Supporting Information). To demonstrate the new method, a 66-sample nanoparticle library of nanocrystalline $Ce_xZr_yY_zO_{2-\delta}$ was produced in <12 h, which is unprecedented in the analogous hydrothermal literature. Furthermore, high resolution PXRD data were obtained for the entire heat-treated library (at 1000 °C/1 h) in less than a day using the new robotic beamline (I11)[14] instrument located at Diamond Light Source (DLS) [video S1 and Figure S1 photographs of the beamline, Supporting Information]. This allowed Rietveld-quality powder X-ray diffraction (PXRD) data collection of the entire 66-sample library in <1 day (Figure S2 for data refinement information and raw data, Supporting Information). Consequently, the authors rapidly mapped out phase behavior and sintering behaviors for the entire library (Table S1 and Ref S2, Supporting Information, and Figure 2).

Experimental Section

Synthesis Methods. The metal salt solutions were prepared as follows: $Y(NO_3)_3 \cdot 6H_2O$ (17.24 g, 0.045 mol), $ZrO(NO_3)_2 \cdot 6H_2O$ (10.41 g, 0.030 mol), and $(NH_4)_2Ce(NO_3)_6$ (24.67 g, 0.045 mol) were accurately weighed and then separately added into 150 mL distilled water in three different beakers, respectively, to give concentrations of 0.3 M for both Ce and Y salts and 0.2 M for the Zr salt. Thereafter, the mole ratios of the 66 compounds were achieved by using a pipet (Eppendorf, U.K.), where the corresponding volumes of the respective metal salt solutions were individually added into the 66 labeled small vials. The compositions as synthesized were based on molecular weights as given on the manufacturer's bottle labels. However, for the Zr-salt, the molecular weight did not include the 6 molecules of water of hydration. Thus, the corrected nominal compositions, as given in Table S2, Supporting Information, are not in precise 10 mol % steps. The actual metal content for each sample obtained by calibrated EDX measurements are listed in Table S3, Supporting Information. The total volume of solutions in each vial was prepared at 6.0 mL, which was just enough for two injections during the experiment. The samples were made in a HiTCH flow synthesis system as described in detail the supplementary section (Ref S1, Supporting Information). The product from the first injection was rejected, while the product from the second injection was collected for use. Between consecutive sample compositions, the HiTCH flow synthesis system was purged by pumping water through the apparatus for ~4 min; during this time, the flow rates were temporarily increased by 25% before restoration of the normal flow rates and reestablishment of thermal equilibrium (see Ref S3, Supporting Information, for information on system validation and recovery of samples).

PXRD Methods. Each of the 45 detectors on Beamline I11[14] were calibrated (using a standard Y_2O_3 sample sintered at 1200 °C for 5 days and measured for 4 h in a 0.5 mm capillary) for relative detector response and precise angular 2θ separation (nominal spacing 2° within a bank of nine detectors and 30° between each of the 5 banks). Diffraction patterns from each detector were corrected for both synchrotron beam decay (using a linear fit to the counts from an in-line X-ray beam monitor) and detector response. Corrected patterns from individual detectors were checked for consistency and merged into a single PXRD pattern covering the 2θ range of 0−155° in various 2θ step sizes, for example, 0.002°, 0.005°, 0.02°, and 0.05°, depending on the degree of peak broadening observed. PXRD data were not used above 90° in 2θ because of initial commissioning problems for detector bank 4.

Results and Discussion

Compared to previous work using continuous hydrothermal flow synthesis (CHFS) reactors (suitable for one or a few samples per day),[2,10,11,18−25] the new HiTCH flow reactor incorporates a Rheodyne injector that is used for the periodic injection of metal salt solution into the system. After each mixture (made from stock metal salt solutions, Ref S2,

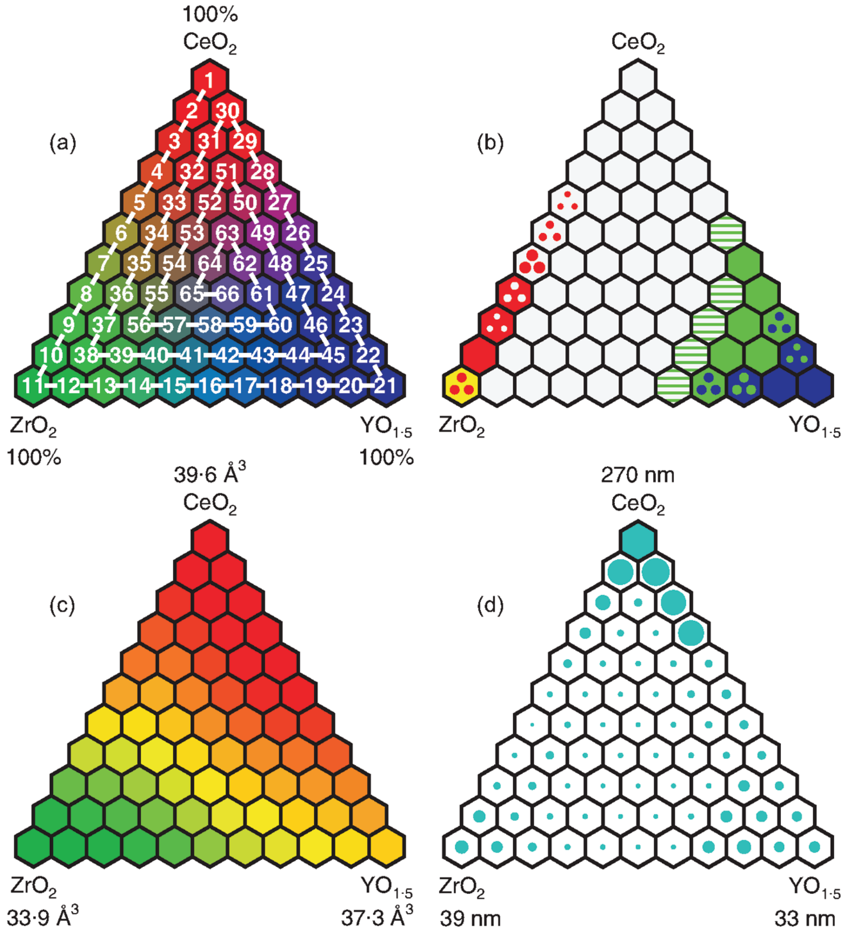

Figure 2. (a) Compositional space for $Ce_xZr_yY_zO_{2-\delta}$ (for $0 \le x, y, z \le 1$). Each hexagon represents a single sample, and the nominal molar content of Ce, Zr, and Y in each sample is proportional to the amount of red, green, and blue color, respectively (Table S1, Supporting Information). Samples are synthesized in sequential order starting at 1 and ending at 66 thus avoiding the possibility of cross contamination for the binary compositions. (b) A simplified phase diagram for $Ce_xZr_yY_zO_{2-\delta}$ as deduced from the synchrotron PXRD data showing the following phase types: fluorite (gray), monoclinic ZrO_2 (yellow), tetragonal ZrO_2 (red), bixbyite (blue), and a 2 × 2 × 2 oxygen-deficient fluorite superstructure (pseudo-Y_2O_3) with oxygen-vacancy ordering (green). Hexagons in a single color indicate single-phase material, while a hexagon with three dots indicates two-phase behavior, and those with striped colors indicate a single-phase region, where there appears to be a smooth transition between fluorite and the 2 × 2 × 2 oxygen deficient fluorite superstructure. (c) Lattice parameter information (Table S1, Supporting Information) obtained from Rietveld-fitted PXRD data converted to mean volume per metal oxide ($MO_{2-\delta}$) unit showing a smooth pseudolinear variation with mole fraction. The volume at each nominal point (in Å^3) for $Ce_xZr_yY_zO_{2-\delta}$ can be approximated by the linear equation: $V = 40.3x + 33.5y + 37.5z$. Refined lattice parameters are consistent with the published comparable literature.[6,17] (d) Relative crystallite size (as indicated by the circle diameters) obtained by application of the Scherrer equation[17] to the strongest PXRD peak (at $2\theta \approx 15°$) for each of the 66 samples (Table S2, Supporting Information). The instrumental contribution to peak broadening was measured using a standard sample of Y_2O_3 (5 days at 1200 °C). The largest crystallite size was obtained for pure CeO_2 and is shown by a filled hexagon. For a−d, the as-prepared nanoparticulate sample library was heat treated at 1000 °C for 1 h in air prior to analysis.

Supporting Information) was fed into the injector, samples were collected as slurries at the exit of the apparatus after a 300 s delay. In all cases herein, the wet nanoparticle slurries from HiTCH flow synthesis were freeze-dried and then the entire 66-sample library was heat-treated at 1000 °C/1 h to give powders ranging from off-white for yttria and zirconia and dark brown for ceria after heat-treatment (Figure 1b). The particle morphologies of as-prepared #6 ($Ce_{0.59}Zr_{0.41}O_{2-\delta}$) was analyzed using high resolution Transmission Electron Microscopy (TEM) images that showed rounded highly crystalline agglomerated particles with a mean particle size of 4.7 ± 0.9 nm (50 particles samples, range 2.2−6.6 nm (Figure 3a and b).

Figure 2a−d summarizes the results in terms of the compositional space defined by the heat-treated samples. The sequential order for producing the 66 samples with the nominal compositions shown represents an idealized route for avoiding the possibility of contamination between binary and ternary systems (Figure 2a). Figure 4 shows the phase diagram including locations of precise compositions and phase boundaries (see Supporting Information Table S3 for exact compositions). The lattice parameter information was converted to mean volume per metal oxide (MO_x) unit and generally shows a smooth approximately linear variation with mole fraction (Figure 2c).

Analysis of PXRD peak broadening[26] can yield useful particle size information for heat-treated samples to infer the extent of sintering. In our heat-treated Ce−Zr−Y system, analysis of peak widths yielded a volume weighted particle size map (Figure 2d). Within the single-phase fluorite domain, the particle size for the seven ceria rich samples, nos. 1−3 and 28−30 are rather large in the range 44 to 270 nm (average = 105 nm). By contrast, the remaining 37 fluorite phase samples (as suggested solely by PXRD) exist

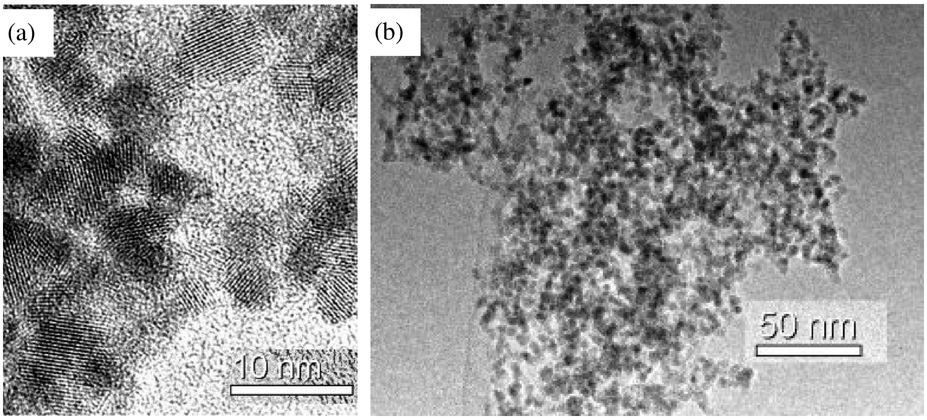

Figure 3. Transmission electron microscope images of as-prepared no. 6 ($Ce_{0.59}Zr_{0.41}O_{2-\delta}$) nanoparticles showing rounded highly crystalline agglomerated particles with a mean particle size of 4.7 ± 0.9 nm (50 particles samples, range 2.2−6.7 nm.

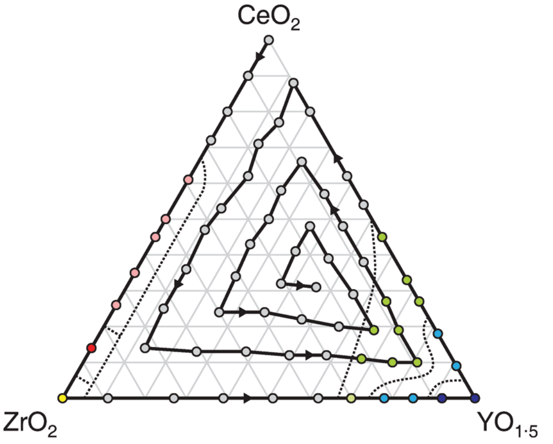

Figure 4. Precision phase diagram as suggested by PXRD showing the actual compositions of the 66 samples, the order of synthesis, and approximate positions of phase boundaries. The different colors represent the following observed structures: gray = single phase fluorite, pink = mixed tetragonal/pseudocubic + fluorite, red = tetragonal pseudo-ZrO_2, yellow = mixture of monoclinic and tetragonal pseudo-ZrO_2, blue = bixbyite, green = 2 × 2 × 2 fluorite (pseudo-Y_2O_3) superstructure as a result of oxygen-vacancy ordering, and cyan = mixture of blue and green phases.

in the narrow particle size range of 13−33 nm (average = 18 nm). The smallest crystallite size was for no. 7 at ~9 nm (middle of the mixed tetragonal/fluorite phase region), which suggests this mixture is highly resistant to grain growth under the heat-treatment conditions (these values contrast to the as-prepared nanopowders, which show crystallite sizes typically in the range 4 to 17 nm (average 8 nm).[26]

Because of the wide range of reported synthesis methods in the literature, which largely concern binary systems rather than entire ternary phase diagrams, direct comparison of similar bulk powders, monoliths, or nanoceramic powders exposed to 1000 °C or so, requires careful interpretation. A discussion of as-prepared nanoceramic samples is published elsewhere.[22,23] Out of the entire 66-sample heat-treated library, the PXRD data suggests that 43 possess the fluorite structure, of which 30 (out of 36) are ternary compositions. Pure CeO_2 (no. 1) is obtained as a cubic fluorite structure (space group $Fm\bar{3}m$), which is consistent with the published literature.[27,28]

In comparison to the previous literature for bulk powdered materials or monoliths,[5] we observe some subtle differences. For example, the literature reports that the tetragonal-pseudocubic phase and the pseudocubic−cubic (fluorite) phase boundary is in the range $z = 0.18$ to 0.19.[17,29] This is in contrast to no. 12 ($Zr_{0.89}Y_{0.11}O_{2-\delta}$), which appears to show only a single-phase fluorite structure (according to PXRD). This could be because of the homogeneity of the solid solution plus the small grain size, which encourages a greater number of oxygen defects and consequently higher-symmetry phases or due to a strain induced transformation. However, since PXRD is insensitive to oxygen-displacive transitions, it is difficult to provide definitive assignments as to whether no. 12 is strictly cubic (fluorite) or pseudocubic. Further Raman analysis suggests that $Zr_{0.89}Y_{0.11}O_{2-\delta}$ is pseudocubic with respect to the local cation symmetry.[22]

Similarly, for the underexplored yttria-doped ceria binary system monoliths, $Ce_xY_zO_{2-\delta}$, recent literature indicates that the fluorite phase exists up to values of $z = 0.30$.[15] Interestingly, our results suggest that the fluorite structure extends up to the range $z = 0.46-0.55$ (nos. 27 and 26 as measured by EDX) in agreement with earlier studies.[5] From the 66 sample library, 6 (out of 36) ternary samples (nos. 43−47 and 60) possess a vacancy-ordered oxygen-deficient fluorite (pseudo-Y_2O_3) superstructure (Figure 2b). Additionally, the binary $Ce_xY_zO_{2-\delta}$ powders nos. 24−26 (EDX measured compositions in the range $z = 0.55$ to 0.73) and the binary no. 17 ($Zr_{0.30}Y_{0.70}O_{2-\delta}$) have the same structure. For the remaining 13 samples, 3 samples appear single phase and 10 are mixed phase. The single phase samples being pure Y_2O_3 (no. 21, bixbyite structure, space group $Ia\bar{3}$) [Figure 5], $Zr_{0.08}Y_{0.92}O_{2-\delta}$ (no. 20), and $Ce_{0.14}Zr_{0.86}O_{2-\delta}$ (no 10) and with a tetragonal (ZrO_2 type) structure. The mixed phase samples can be separated into four distinct categories. Pure ZrO_2 (no. 11) is a ~86:14 mixture of monoclinic (space group $P2_1/c$) and tetragonal (space group $P4_2/nmc$) phases, which is similar with an earlier report by the authours.[30]

In the literature, pure bulk zirconia exists as monoclinic (below 1167 °C), although it is known that fine-grained zirconia nanoparticles (<30 nm diameter) can exist with a tetragonal structure at room temperature.[28] For the five mixed-phase $Ce_xZr_yO_{2-\delta}$ samples (nos. 5−9), with increasing Ce^{4+} content, there is a switch from majority tetragonal to majority fluorite structure occurring between nos. 7 and 8. In the majority fluorite phase from no. 7 to no. 5, the minor

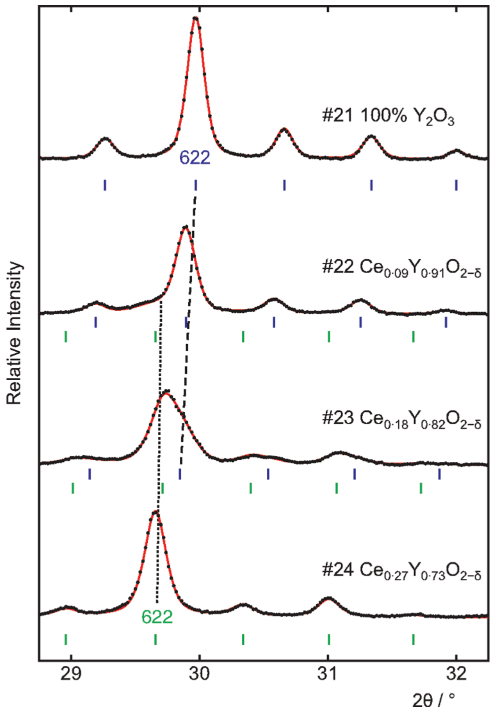

Figure 5. Plots showing selected expanded regions of the Rietveld fits for nos. 21, 22, 23, and 24 (these are single-phase bixbyite (Y_2O_3) for no. 21, a 2-phase mixture of a 2 × 2 × 2 fluorite superstructure (pseudo-Y_2O_3) with oxygen-vacancy ordering and bixbyite for nos. 22 and 23, and single-phase fluorite superstructure for no. 24) to demonstrate the existence of single phase (nos. 21 and 24) and mixed phase (for nos. 22 and 23) behavior.

phase cannot be identified by PXRD alone but Raman spectroscopic analysis has shown this is pseudocubic t'', with peaks located at 264, 457(s), and 615 cm^{-1}, 296, 460(s), and 620 cm^{-1}, and 304, 459(s), and 624 cm^{-1}, respectively.[22] There are 2 mixed-phase $Zr_yY_zO_{2-\delta}$ samples because of the transition from majority vacancy-ordered oxygen-deficient fluorite (pseudo-Y_2O_3) to bixbyite (Y_2O_3) structure (nos. 18 and 19) as shown in Figure 2b. There is a very similar distinct change in structure for the two mixed-phase $Ce_xY_zO_{2-\delta}$ samples nos. 23 (average composition $Ce_{0.18}Y_{0.82}O_{2-\delta}$) and 22 (average composition $Ce_{0.09}Y_{0.91}O_{2-\delta}$) that is in contrast to an earlier report suggesting that the yttria-rich corner is single-phase bixbyite.[5]

Conclusions

A new High-Throughput Continuous Hydrothermal (HiTCH) flow synthesis method, which has enabled unprecedented synthesis of large numbers of nanoceramics. The technology enabled an entire ceria−zirconia−yttria ternary phase diagram (66-sample libraries) to be made in less than a day. Subsequently, the use of a brand new high resolution powder diffraction facility at Diamond was used to gain high quality diffraction data on the entire heat-treated library. The speed, quantity, and quality of data obtained by our new approach offers an exciting new development which will allow structure−property relationships to be accessed for nanoceramics in reasonable time periods.

Acknowledgment. EPSRC is thanked for funding the “High-Throughput Nanoceramics Discovery Project” (Grant reference EP/D038499/1); members of the project who are acknowledged for helpful discussions and input include Prof. Z. X Guo, Dr S. Kellici, Dr K. Gong, and Z. Zhang. STFC are also thanked for funding the Diamond Light Source Facility at Beamline I11. Prof. A.N. Fitch (European Synchrotron Radiation Facility, ESRF) is thanked for his useful advice during the design and construction phases of Beamline I11. N.J. Mordan is thanked for assistance with the EDX elemental analyses. J.K.C., C.C.T., and J.A.D. contributed equally to this work.

Supporting Information Available. Details of the HiTCH apparatus design, miscellaneous chemical information, images of the I11 diffractometer showing the 45-analyzer crystals and detectors and autosampler, the PXRD data from each of the 66 heat-treated nanoceramics, phase composition, and unit-cell parameters from Rietveld refinement with derived volume per metal oxide unit, Z, the number of $MO_{2-\delta}$ formula units per unit cell, table of relative crystallite sizes (nm) obtained by application of the Scherrer equation to the strongest PXRD peak (at $2\theta \approx 15°$), elemental analytical data, and a video showing the I11 diffractometer robot in operation. This material is available free of charge via the Internet at http://pubs.acs.org.

References and Notes

(1) Pitcher, M. W. *Science* **2006**, *313*, 300.
(2) Boldrin, P.; Hebb, A. K.; Chaudhry, A. A.; Otley, L.; Thiebaut, B.; Bishop, P.; Darr, J. A. *Ind. Eng. Chem. Res.* **2007**, *46*, 4830.
(3) Esch, F.; Fabris, S.; Zhou, L.; Montini, T.; Africh, C.; Fornasiero, P.; Comelli, G.; Rosei, R. *Science* **2005**, *309*, 752.
(4) Longo, V.; Podda, L. *J. Mater. Sci.* **1981**, *16*, 839.
(5) Deportes, C.; Robert, G.; Forestie, M. *Electrochim. Acta* **1971**, *16*, 1003.
(6) Goodenough, J. B. *Nature* **2008**, *404*, 821.
(7) Wright, C. S.; Walton, R. I.; Thompsett, D.; Fisher, J.; Ashbrook, S. E. *Adv. Mater.* **2007**, *19*, 4500.
(8) Martin, P.; Grandjean, S.; Valot, C.; Carlot, G.; Ripert, M.; Blanc, P.; Hennig, C. *J. Alloys Compd.* **2007**, *444*, 410.
(9) Sickafus, K. E.; Grimes, R. W.; Valdez, J. A.; Cleave, A.; Tang, M.; Ishimaru, M.; Corish, S. M.; Stanek, C. R.; Uberuaga, B. P. *Nat. Mater.* **2007**, *6*, 217.
(10) Chaudhry, A. A.; Goodall, J. B. M.; Vickers, M.; Cockcroft, J. K.; Rehman, I.; Knowles, J. C.; Darr, J. A. *J. Mater. Chem.* **2008**, *18*, 5900.
(11) Zhang, Z.; Brown, S.; Goodall, J. B. M.; Weng, X.; Thompson, K.; Gong, K.; Kellici, S.; Clark, R. J. H.; Evans, J. R. G.; Darr, J. A. *J. Alloys Compd.* **2009**, *476*, 451.
(12) Kaspar, J.; Di Monte, R.; Fornasiero, P.; Graziani, M.; Bradshaw, H.; Norman, C. *Top. Catal.* **2001**, *16*, 83.
(13) Ozawa, M. *J. Alloys Compd.* **1998**, *275*−*277*, 886.
(14) Tang, C. C.; Thompson, S. P.; Hill, T. P.; Wilkin, G. R.; Wagner, U. H. *Z. Kristallogr. Suppl.* **2007**, *26*, 153.
(15) Ikuma, Y.; Kamiya, M.; Nagasawa, S. *Solid State Electrochemistry*; Proceedings of the 26th International Symposium on Material Science, Roskilde, Denmark; 2005, 241.
(16) Cabanas, A.; Darr, J. A.; Lester, E.; Poliakoff, M. *J. Chem. Soc., Chem. Commun.* **2000**, 901.
(17) Yashima, M.; Ohtake, K.; Kakihana, M.; Arashi, H.; Yoshimura, M. *J. Phys. Chem. Solids* **1996**, *57*, 17.
(18) Weng, X.; Boldrin, P.; Abrahams, I.; Skinner, S. J.; Kellici, S.; Darr, J. A. *J. Solid State Chem.* **2008**, *181*, 1123.

(19) Weng, X.; Boldrin, P.; Abrahams, I.; Skinner, S. J.; Darr, J. A. *Chem. Mater.* **2007**, *19*, 4382.

(20) Darr, J. A.; Poliakoff, M. *Chem. Mater.* **1999**, *99*, 495.

(21) Chaudhry, A. A.; Haque, S.; Kellici, S.; Boldrin, P.; Rehman, I.; Fazal, A. K.; Darr, J. A. *J. Chem. Soc., Chem. Commun.* **2006**, 2286.

(22) Weng, X. W. Continuous hydrothermal syntheses of nanoceramics towards better oxide ion and electronic conductors. PhD Thesis, Queen Mary University of London, London, 2008.

(23) Middelkoop, V.; Boldrin, P.; Peel, M.; Buslaps, T.; Barnes, P.; Darr, J. A.; Jacques, S. *Chem. Mater.* **2009**, *21*, 2430.

(24) Zhang, Z.; Goodall, J. B. M.; Morgan, D. J.; Brown, S.; Clark, R. J. H.; Knowles, J. C.; Mordan, N. J.; Evans, J. R. G.; Carley, A. F.; Bowker, M.; Darr, J. A. *J. Mater. Chem.* **2009**, *29*, 2343.

(25) Weng, X.; Perston, B.; Wang, X.; Abrahams, I.; Lin, T.; Yang, S.; Evans, J. G. R.; Morgan, D. J.; Carley, A. F.; Bowker, M.; Knowles, J. C.; Rehman, I.; Darr, J. A. *Appl. Catal. B: Environ.* **2009**, *90*, 405.

(26) Le Bail, A. In *Powder Diffraction Theory and Practice*; Dinnibier, R. E., Billinger, S. J. L., Eds.; RSC: Cambridge, U.K., 2008; p 142.

(27) Yashima, M.; Arashi, H.; Kakihana, M.; Yoshimura, M. *J. Am. Chem. Soc.* **1994**, *77*, 1067.

(28) Zhang, F.; Chen, C. H.; Hanson, J. C.; Robinson, R. D.; Herman, I. P.; Chan, S. W. *J. Am. Chem. Soc.* **2006**, *89*, 1028.

(29) Yashima, M.; Kakihana, M.; Yoshimura, M. *Solid State Ionics* **1996**, *86*−*8*, 1131.

(30) Cabanas, A.; Darr, J. A.; Lester, E.; Poliakoff, M. *J. Mater. Chem.* **2001**, *11*, 561.

CC900041A